DOE/ET-53088-272 IFSR #272

Incompressible Description of Rayleigh-Taylor Instabilities in Laser Ablated Plasmas

H. J. Kull

Institute for Fusion Studies
The University of Texas at Austin
Austin, Texas 78712

March 1987

Incompressible Description of Rayleigh-Taylor Instabilities in Laser Ablated Plasmas

H.J. Kull[a]

Institute for Fusion Studies
The University of Texas at Austin
Austin, Texas 78712

January 1987

Abstract

The Rayleigh-Taylor instability of a plane ablative heat wave is investigated. A local incompressible stability analysis with self-consistent steady-state and instability dynamics is described. Growth rates are obtained as eigenvalues of the instability boundary-value problem and the structure of the eigenmodes is discussed. The ablative instability cutoff is evaluated over a wide parameter range and representative conditions for laser-driven ablation are identified. For comparable profiles excellent agreement with both previous compressible and sharp-boundary results is found.

[a] *Permanent address: Technische Hochschule Darmstadt, Institut für Angewandte Physik, D-6100 Darmstadt, FRG*

I. Introduction

In most laser fusion concepts one attempts to achieve fusion conditions by ablative acceleration of high-aspect-ratio shells. One of the crucial issues in this context is the hydrodynamical stability of the ablation process. Rayleigh-Taylor (RT) instabilities, arising from inverted density gradients, are likely to occur and have been reported in a number of investigations.[1–4]

In the present study we examine a reduced description of the ablation front instability. The purpose is to include in a simplified but self-consistent manner the effects of mass ablation and heat flow into the classical treatment of Rayleigh-Taylor instability. Our main assumption is that the instability evolution can be understood on the basis of incompressible theory. Evidently, this limits our discussion to subsonic ablation fronts, which are widely enough separated from the sonic-point region. The incompressible fluid approach has been discussed in detail recently and applied to idealized ablation fronts with infinitely sharp boundaries.[5] In the present study the latter restriction is removed and the treatment is generalized to diffuse boundary layers. Numerical calculations for self-consistent steady-state flows are presented, which can confirm the validity of a local incompressible stability analysis.

Our procedure of calculating the instability growth rates is described in Sec. II. We consider an eigenmode analysis and determine the growth rates as eigenvalues of the instability boundary-value problem. The corresponding solubility condition is expressed in close analogy to our previous result and reduces to this case for the sharp boundary model. Some important simplifications for the numerical work have been gained by (i) using analytic solutions for the asymptotic boundary regions, (ii) smooth variables in the boundary layer, and (iii) by integrating from the ablation front towards lower densities, where only two independent numerical solutions are required.

The computational results are discussed in detail in Sec. III. For an incompressible model in slab geometry the solutions can be distinguished by a single parameter Γ, which denotes a dimensionless acceleration. The instability dispersion relations

are given for a wide range of parameter values. While ablative effects are small for long wavelengths, they tend to dominate and even stabilize the flow for short wavelengths. The cutoff wave number for marginal stability is therefore of special theoretical and practical interest. We determine the stability boundary as a function of the instability parameter. It indicates improved stability behavior both for very small and very large parameter values. Similar observations have been made previously for the idealized sharp boundary model. We also discuss the spatial structure of the unstable eigenmodes both in the classical and ablative instability regime. Typical mode structures are explained by considering the mass, momentum and energy flows as well as the density in the unstable region.

The mathematical sharp boundary model depends crucially on the choice of boundary conditions. To confirm conditions used previously,[5] we make a detailed comparison with the present numerical method. For a class of finite-thickness layers the convergence towards the step-profile limit can be explicitly demonstrated. The maximum thickness consistent with the sharp-boundary limit, however, is found rather small and actually comparable with the minimum scale length at the ablation front. This shows clearly the need for a diffuse boundary treatment. Although the sharp boundary model is not rigorously valid for consistent profiles, we explain how these results may be applied to model diffuse boundary layers. Introducing the profile-step near the perturbation maximum is shown to lead to satisfactory agreement both for the growth rates and the mode structures.

Next we discuss to some extent the occurrence of subsonic fronts and the respective values of Γ in the laser fusion context. For this purpose we consider more global steady ablation models extending up to the sonic point region.[6] From this analysis it follows that ablation front conditions can vary appreciably, depending on a parameter μ, which is the ratio of the typical penetration depth of the heat wave over the typical scale height of the slab. For steep fronts, $\mu \ll 1$, the values of Γ can become very small, corresponding to the more favorable instability regime. In this case it is however likely that the instability zone overlaps the sonic point region, so that our analysis here can only be considered preliminary. For more extended heat

waves, $\mu \approx 1$, the ablation front is usually well separated from the sonic-point and the typical values of Γ are found in the interval $0.1 - 0.3$.

Finally, we compare the present model with previous computations, solving the complete set of compressible fluid equations.[6-7] In the parameter range $\Gamma = 0.1 - 0.2$, where such results are available, we find excellent agreement for the growth rates in the ablative regime. This strongly supports that the incompressible description yields actually accurate predictions.

II. Growth Rate Calculations

To investigate the RT instability with ablation, we first consider steady ablation in the incompressible flow regime. A plane heat wave is assumed propagating in the y-direction such that in an accelerated coordinate frame the flow becomes steady and subject to an effective gravitational acceleration $\mathbf{g} = (0, -g, 0)$. The flow variables are the velocity $\mathbf{v} = (0, -v, 0)$, density ρ, pressure p, and temperature T. Following previous work[5] we neglect compressibility effects, by using an isobaric approximation to the energy equation,

$$\nabla \cdot (\mathbf{v} + \chi \nabla \rho / \rho) = 0. \tag{1}$$

The coefficient of thermal diffusivity χ is assumed as a power law, $\chi = \text{const}\, T^{\nu+1}$ of temperature. If not stated differently we use $\nu = 2.5$, corresponding to classical electronic heat conduction. It is convenient to introduce dimensionless variables $\bar{X} = X/X_1$, where X_1 denotes the asymptotic value approached by the variable X inside the cold slab, and a dimensionless coordinate $\xi = y v_1/\chi_1$. Then we have $\bar{v} = \bar{T} = 1/\bar{\rho}$ and Eq. (1) can be written in the form,

$$\frac{d}{d\xi}\bar{\rho} = \bar{\rho}^{\nu+1}(1 - \bar{\rho}). \tag{2}$$

The density profiles obtained from Eq. (2) depend only on the heat conductivity exponent ν and increase with ξ up to the asymptotic value $\bar{\rho} = 1$ (Fig. 1). Note that the density gradient is opposed to the gravitational acceleration, corresponding to a Rayleigh-Taylor unstable configuration.

To analyze the stability of the steady-state we consider now a normal mode ansatz with perturbations $\delta X = \delta X(y)\exp(nt+ikx)$ for each flow variable X. The linearized equations for mass, momentum and energy conservation yield,

$$\begin{aligned}
\frac{d}{dy}(\rho\delta v_y - v\delta\rho) + n\delta\rho + ik\rho\delta v_x = 0 \ , \\
\frac{d}{dy}(\rho v\delta v_x) - n\rho\delta v_x - ik\delta p = 0 \ , \\
\frac{d}{dy}(v^2\delta\rho - 2\rho v\delta v_y + \delta p) + n(\rho\delta v_y - v\delta\rho) - ik\rho v\delta v_x + g\delta\rho = 0 \\
\frac{d}{dy}\left[\delta v_y + \frac{d}{dy}\left(\chi\frac{\delta\rho}{\rho}\right)\right] + ik\delta v_x - k^2\chi\frac{\delta\rho}{\rho} = 0 \ .
\end{aligned} \tag{3}$$

For studying the transition to a sharp boundary it is convenient to use variables which stay continuous across a boundary layer of zero thickness. In our model such variables are,

$$\begin{aligned}
Y_1 &= \bar{\rho}\delta\bar{v}_y - \bar{v}\delta\bar{\rho} \\
Y_2 &= i\delta\bar{v}_x \\
Y_3 &= \bar{v}^2\delta\bar{\rho} - 2\delta\bar{v}_y + \delta p/(\rho_1 v_1^2) \\
Y_4 &= \bar{\chi}\delta\bar{\rho}/\bar{\delta} \\
Y_5 &= \delta\bar{v}_y + \frac{d}{d\xi}Y_4
\end{aligned} \tag{4}$$

where we used the notation of Eq. (2). Note that Y_1 represents the mass flow, $-iY_2$ the x-momentum flow, Y_3 the y-momentum flow, while $\frac{d}{d\xi}Y_4$ is proportional to the heat and Y_5 to the energy flow. Transforming Eq. (3) to the variables (4) and defining $\sigma = n\chi_1/v_1^2$, $\kappa = k\chi_1/v_1$, $\Gamma = g\chi_1/v_1^3$ one obtains the first order system,

$$\frac{d}{d\xi}\mathbf{Y} = \mathbf{M}(\sigma,\kappa,\Gamma,\nu,\bar{\rho})\cdot\mathbf{Y} \tag{5}$$

with

$$\mathbf{Y} = \begin{pmatrix} Y_1 \\ Y_2 \\ Y_3 \\ Y_4 \\ Y_5 \end{pmatrix} \qquad \mathbf{M} = \begin{pmatrix} 0 & -\kappa\bar{\rho} & 0 & -\sigma\bar{\rho}^{\nu+2} & 0 \\ -2\kappa/\bar{\rho} & \sigma\bar{\rho} & -\kappa & -\kappa\bar{\rho}^{\nu} & 0 \\ -\sigma & \kappa & 0 & \Gamma\bar{\rho}^{\nu+2} & 0 \\ -1/\bar{\rho} & 0 & 0 & -\bar{\rho}^{\nu} & 1 \\ 0 & -\kappa & 0 & \kappa^2 & 0 \end{pmatrix} .$$

The unstable perturbations tend to be localized near the maximum density gradient. We are therefore looking for solutions of Eq. (5), which become evanescent at the boundaries $|\xi| \to \infty$. The growth rate σ is obtained as an eigenvalue of this boundary value problem. Generally it will depend on the wave number κ as well as on the parameters Γ and ν. We also remark that our definition of Γ agrees with that of F in Ref. 5.

To impose the boundary conditions more specifically, we assume boundary regions for $\xi > 0$ and $\xi < -d$. In these regions the flow is considered locally homogeneous and the flow variables are denoted by an index 1 and 2, respectively. For the profile (2) the origin $\xi = 0$ has been chosen such, that $\bar{\rho}(0) = 0.999$, which is nearly the asymptotic value $\bar{\rho} = 1$ approached at $\xi = +\infty$. We therefore set $\bar{\rho}(0) = \bar{\rho}_1 = \bar{v}_1 = \bar{\chi}_1 = 1$. The layer thickness d should satisfy the requirement that the growth rates do not change significantly when d is further increased. We find that this criterion is well satisfied for $\kappa d \gtrsim 1.5$ and have chosen $\kappa d = 2.5$ for most calculations. The solutions $\mathbf{Y}_1$ of Eq. (5) tending to zero in region 1 satisfy at $\xi = 0$ the initial conditions,

$$\mathbf{Y}_1(0) = \begin{pmatrix} 1 \\ 1 \\ \sigma/\kappa - 1 \\ 0 \\ 1 \end{pmatrix} a + \begin{pmatrix} -1 - r_1 \\ -s_1 \\ t_1 \\ 1 \\ \kappa^2 h_1 \end{pmatrix} b \ . \tag{6a}$$

Likewise solutions $\mathbf{Y}_2$, tending to zero in region 2 satisfy at $\xi = -d$ the initial conditions,

$$\mathbf{Y}_2(-d) = \begin{pmatrix} 1 \\ -1/\bar{\rho}_2 \\ -\sigma/\kappa - 1/\bar{\rho}_2 \\ 0 \\ 1/\bar{\rho}_2 \end{pmatrix} c + \begin{pmatrix} 1 \\ -\sigma/\kappa \\ -2/\bar{\rho}_2 \\ 0 \\ 1/\bar{\rho}_2 \end{pmatrix} d + \begin{pmatrix} -\bar{\rho}_2^{\nu+1}(1 + r_2) \\ -\bar{\rho}_2^{\nu} s_2 \\ \bar{\rho}_2^{\nu} t_2 \\ 1 \\ \kappa^2 h_2 \end{pmatrix} e \ . \tag{6b}$$

Here a, b, c, d, e represent arbitrary constants and,

$$r = (q - \kappa^2 h)/\bar{\rho}^\nu$$

$$s = -\kappa(1 - qh)/\bar{\rho}^\nu$$

$$t = 1 + 2r + (s/\kappa)(q - \bar{\rho}\sigma)$$

$$h = \Gamma/(\sigma - q/\bar{\rho})^2$$

$$q_1 = -\tfrac{1}{2} - (\tfrac{1}{4} + \sigma + \kappa^2)^{1/2}$$

$$q_2 = -\tfrac{1}{2}\bar{\rho}_2^\nu + (\tfrac{1}{4}\bar{\rho}_2^{2\nu} + \bar{\rho}_2^{\nu+1}\sigma + \kappa^2)^{1/2} \ .$$

To obtain solutions which satisfy both Eq. (6a) and Eq. (6b) we calculate $\mathbf{Y}_1(-d)$, by integrating Eq. (5) with the initial conditions $\mathbf{Y}_1(0)$. The jump of $\mathbf{Y}_1$ across the layer, $-d < \xi < 0$, is generally written in the form,

$$\mathbf{Y}_1(0) - \mathbf{Y}_1(-d) = a\mathbf{K} + b\mathbf{J} \ ,$$

where $\mathbf{K}$ and $\mathbf{J}$ denote the jumps of the particular solutions $a = 1$, $b = 0$ and $a = 0$, $b = 1$, respectively. Matching now $\mathbf{Y}_1$ to $\mathbf{Y}_2$ at $\xi = -d$ yields

$$\mathbf{Y}_1(0) - \mathbf{Y}_2(-d) = a\mathbf{K} + b\mathbf{J} \ . \tag{7}$$

This is a homogeneous vector system for the unknown constants a, b, c, d, e. Setting the determinant of the coefficient matrix equal to zero, there follows the solubility condition,

$$(A - \bar{\rho}_2 D)\left[\beta - \gamma + \left(2 + \bar{\rho}_2 \frac{\sigma}{\kappa}\delta\right)\right] - (\alpha - \bar{\rho}_2\delta)\left[B - C + \left(2 + \bar{\rho}_2 \frac{\sigma}{\kappa} D\right)\right] = 0 \tag{8}$$

with the substitutions,

$$A = -(1 + r_1) + \bar{\rho}_2^{\nu+1}(1 + r_2)(1 - J_4) - J_1$$

$$B = -s_1 + \bar{\rho}_2^\nu s_2(1 - J_4) - J_2$$

$$C = -t_1 + \bar{\rho}_2^\nu t_2(1 - J_4) + J_3$$

$$D = \kappa^2 h_1 - \kappa^2 h_2(1 - J_4) - J_5$$

$$\alpha = 1 - K_1 - \bar{\rho}_2^{\nu+1}(1 + r_2)K_4$$

$$\beta = 1 - K_2 - \bar{\rho}_2^\nu s_2 K_4$$

$$\gamma = 1 - \frac{\sigma}{\kappa} + K_3 - \bar{\rho}_2^\nu t_2 K_4$$

$$\delta = 1 - K_5 + \kappa^2 h_2 K_4 \ .$$

Equation (8) determines the possible growth rates σ. We used a standard numerical algorithm to calculate the zeros in Eq. (8), iteratively. For each estimate of σ one has to evaluate the jumps $\mathbf{K}$ and $\mathbf{J}$, by integrating Eq. (5). For a sharp boundary model one has $\mathbf{K} = \mathbf{J} = 0$ and Eq. (8) reduces to the solubility condition discussed previously.[5]

III. Discussion of Results

The numerical procedures described in the preceding section now can be applied to calculate the instability growth rates for given density profiles $\bar{\rho} = \bar{\rho}(\xi)$ and given values of the instability parameter Γ and the heat conductivity exponent ν. In this section we discuss the results obtained for different profile models. Furthermore the instability parameter Γ is evaluated for some representative steady-flow conditions and the results of the present reduced fluid model are compared with previous work.

A. Diffuse Boundary Model

Let us first consider a diffuse boundary, with the density profile given self-consistently by Eq. (2). Detailed numerical results for this case are presented in Figs. 2-4. The growth rate curves $\sigma = \sigma(\kappa)$ are shown in Fig. 2 for different values of Γ and ν. The qualitative behavior can be understood by noticing that ablative modifications become negligible at small wave numbers. The asymptotic behavior for $\kappa \rightarrow 0$ is therefore described by the well known *RT* result $\sigma \propto (\Gamma\kappa)^{1/2}$. With increasing wave numbers both the convection rate $\kappa\bar{v}$ and the thermal diffusion rate $\kappa^2\bar{v}^\nu$ increase faster than the instability growth rate. Ultimately, at large wave numbers this gives rise to the instability cutoff, observed in Fig. 2. The cutoff wave number κ_c as a function of Γ is presented in Fig. 3. Wave numbers above the stability boundary $\kappa = \kappa_c(\Gamma)$ are stable, while those below are unstable. The observed increase of κ_c with Γ is due to the Γ-dependence of the *RT* growth rate. We remark that κ_c grows slightly faster than Γ for $\Gamma \lesssim 1$ and slightly slower than $\sqrt{\Gamma}$ for $\Gamma \gtrsim 1$.

According to the present model favorable regimes for ablative acceleration may be found both for small and large Γ values. Let us compare configurations with given

ablation pressure p_1, slab density ρ_1 and velocity v_1. Estimating the foil thickness d_f by the hydrostatic relation $p_1 = \rho_1 g d_f$ yields $k_c d_f = (\kappa_c/\Gamma) p_1/(\rho_1 v_1^2)$. The major stability constraint $k_c d_f \lesssim 1$ scales with the ratio κ_c/Γ. The latter reaches a maximum of about 0.18 at $\Gamma \approx 0.5$ but can be less than 10^{-2} for $\Gamma \lesssim 10^{-2}$ and $\Gamma \gtrsim 10^2$.

Let us finally discuss the typical spatial structure of the eigenmodes. The variables Y_i as defined by Eq. (4) are shown in Fig. 4 as a function of ky. Three widely separated wave numbers have been selected to demonstrate the conditions in the classical instability regime (a), near maximum growth (b), and near the cutoff (c). Note that the solutions are well localized near the ablation front at $y = 0$, reaching their maximum generally above $ky = -1$. The density perturbation Y_4 has been chosen negative, corresponding to a surface region, where the isodensity contours are rising in the y-direction. Its magnitude decreases strongly with increasing wave numbers as can be seen by noting the different normalizations of Y_4 in (a)-(c). While both the mass flow Y_1 and the energy flow Y_5 are found positive, the transverse velocity Y_2 reverses sign across the boundary, indicating shear motion as predicted by standard *RT* theory. The momentum flow normal to the surface Y_3 also changes sign for small wave numbers (a), but positive flow amplitudes become reduced near maximum growth (b) and disappear completely near the cutoff (c).

B. Sharp Boundary Model

For reasons of analytic simplicity it is much more convenient to study a sharp boundary model instead of the diffuse boundary layer given by Eq. (2). This approach allows the derivation of exact dispersion relations and represents an instructive example for the stabilization problem. Evidently, however, these results require further explanation, when the relationship between the sharp and diffuse boundary treatment is considered. For this purpose we now discuss in detail the thin-boundary-layer approximation and compare its predictions with diffuse boundary layer results.

We first wish to confirm that the sharp boundary model actually becomes

valid as a thin-layer limit. To examine the convergence, we assume a boundary layer, $-d < \xi < 0$, with a linear density variation, $\bar{\rho} = 1 + (1 - \bar{\rho}_2)\xi/d$, and consider a sequence of profiles with decreasing layer width d. For a specific case the parameters $\bar{\rho}_2 = 0.1$, $\Gamma = 0.1$ and $\kappa = 0.001$ have been chosen. The calculations, as presented in Fig. 5, show that the maximum layer thickness consistent with the step-profile approach is $d_m \approx 1$. If the layer is much thinner (a) the variables Y_i are continuous across the density jump, but they vary inside the boundary layer for $d \gtrsim 1(c)$. We remark that the limiting thickness $d_m = 1$ is extremely small compared with the inverse transverse wave number $\kappa^{-1} = 1000$. This circumstance can be understood by noticing that d_m is required to satisfy the more restrictive condition, $|qd_m| \lesssim 1$, where q is any wave number along the y-direction, allowed by the asymptotic boundary regions. In the present model the maximum wave number is that of the density perturbation in the region $\xi > 0$ and, from Eq. (6), is given by $q = q_1 \approx -1$. Accordingly, one has $d_m \approx 1$ even in the large wavelength limit, where $\kappa \ll 1$. It may also be instructive to compare the smooth variables Y_i with the more usual flow variables. From Fig. 6 it can be seen that $\delta\rho$, δp and δv_y, as obtained by inverting Eq. (4), vary rapidly in the boundary layer interior, where the variables Y_i are approximately constant.

As we have seen, the maximum allowable width in the thin-layer-approximation is the scale length χ_1/v_1 of the density perturbation. But this is also about the minimum gradient scale length of the steady-state profile (2), and therefore the sharp boundary model is strictly not applicable to this case. In a less rigorous way, however, step-profiles may be used to model a diffuse profile with good qualitative agreement of results. This follows from the observation that for given parameters Γ, ν and κ one can always choose a density ratio $\bar{\rho}_2$ in the sharp boundary model such that the growth rate is the same as for a diffuse boundary. To justify such a comparison, one may think of asymptotic boundary regions, which are continued into the boundary layer up to the region, where the perturbation maximum is assumed. There the profile-step is introduced, with a step-height comparable with the local density of the boundary layer. Let us now adopt this viewpoint and

compare the field structures of Fig. 4 with those of step-profiles with equal growth rates. Step-profile results with corresponding values of Γ, ν, κ and σ are represented in Fig. 7. Here the density ratio $\bar{\rho}_2$ is 0.17 in (a), 0.25 in (b) and 0.4 in (c). Inside the diffuse boundary layer these values of $\bar{\rho}$ are assumed at the points where $ky = 0.1$, 0.14 and 0.29, resepectively. According to Fig. 4 this is about the region of the maximum of Y_3. Comparing now the eigenmodes of Fig. 4 and Fig. 7 one finds a naturally smoother behavior for the diffuse boundary with larger amplitudes for the density perturbation Y_4. But the main features are remarkably similar. The decrease of positive amplitudes of Y_3 with increasing κ is well reproduced by the step-model. Also Y_2, which is continuous across the step, reverses sign downstreams. Only very close to the cutoff (c) the eigenfunctions show a more sensitive profile dependence.

C. Steady Ablation Fronts

The present instability analysis applies to any local steady-state near the ablation front. To discuss the conditions for such local steady-states, we now consider steady-states on the larger compressible scale height of the system. These more global models allow us to evaluate representative ablation front parameters and give some estimates for the range of applicability of the incompressible fluid approach.

We consider steady flows for an ideal gas with particle mass m and adiabatic index γ. The isothermal sonic point, where $v^2 = T/m$, will be denoted by a subscript s and the ablation front, where $\frac{dv}{dy} = 0$, by a subscript 1. Normalizing T by T_s and lengths and times by v_s^2/g and v_s/g, respectively, the steady state fluid equations for the slab geometry of Sec. II assume the form

$$\begin{aligned} \frac{v'}{v}(T - v^2) &= 1 + T' \\ T + \frac{\gamma - 1}{\gamma}\Big(\frac{v^2}{2} + y\Big) + \mu T^\nu T' &= C \ . \end{aligned} \tag{9}$$

These are coupled first-order equations for the velocity and temperature profiles with two parameters $\mu = \chi_s g/v_s^2$ and C. Before looking at some specific cases, we

wish to make a few remarks on the general steady-state problem. The solutions of Eq. (9) may be classified according to their behavior near the sonic point, $v = T = 1$, which is a singular point of Eq. (9). For this purpose it is more convenient to consider variables $y(v)$ and $T(v)$ depending on v. Transforming Eq. (10), one finds for $dy/dv = 1/v'$ and $dT/dv = T'/v'$ the equations,

$$\begin{aligned} D\frac{dy}{dv} &= -\mu T^{\nu} B \\ D\frac{dT}{dv} &= (D + \mu T^{\nu})B \end{aligned} \tag{10}$$

with

$$B = \frac{T - v^2}{v} \ , \ D = T + \frac{\gamma - 1}{\gamma}\Big(\frac{v^2}{2} + y\Big) - \mu T^{\nu} - C \ .$$

We are looking for flows describing a supersonic-subsonic transition with increasing y. Consequently $\frac{dy}{dv} < 0$, and B and D always must have the same signs. Especially, across the sonic point, where B reverses sign, the same must hold for D. This can happen in the singular case, where $D = 0$ for $v = T = 1$. The constraint, $D = 0$, then restricts the constant C to the value,

$$C = 1 + \frac{\gamma - 1}{\gamma}\big(\tfrac{1}{2} + y_s\big) - \mu \ , \tag{11}$$

giving rise to a one-parameter family of solutions depending on μ only. More generally, however, D may change sign discontinuously, if an energy source is assumed at the sonic point. Such a source may model energy deposition by a laser beam and changes the value of C discontinuously across the sonic point. In this more general case one has $D \neq 0$ as $v \to 1$ and a two-parameter family of solutions depending on μ and C can be obtained.

To distinguish these two cases more explicitly we consider a series expansion of the form,

$$\begin{aligned} y &= y_s + a\delta v + b\delta v^2 \\ T &= 1 + c\delta v + d\delta v^2 \\ v &= 1 + \delta v \\ D &= D_0 + D_1\delta v \ . \end{aligned} \tag{12}$$

Inserting Eq. (12) into Eq. (10) the orders 0(1) and $0(\delta v)$ yield the system of equations,

$$\begin{aligned} D_0 a &= 0 \\ D_0 c &= 0 \\ D_1 a + 2D_0 b + \mu(c-2) &= 0 \\ D_1 c + 2D_0 d - (\mu + D_0)(c-2) &= 0 \end{aligned} \tag{13}$$

$$D_0 = 1 + \frac{\gamma-1}{\gamma}(\tfrac{1}{2} + y_s) - \mu - C \;\; ; \;\; D_1 = (1-\mu\nu)c + \frac{\gamma-1}{\gamma}(a+1) \;\; .$$

In the regular case, $D_0 \neq 0$, both y and T are found to approach the sonic point with zero slopes,

$$a = c = 0 \;\; , \;\; b = \mu/D_0 \;\; , \;\; d = -(1+b) \;\; . \tag{14}$$

In the singular case, $D_0 = 0$, the derivatives of y and T generally do not vanish, but two solutions with different slopes branch at the sonic point,

$$\begin{aligned} c &= -a \\ \frac{1}{a} &= -\tfrac{1}{4}\left(1 + \frac{1-\gamma}{\gamma\mu}\right) \mp \left\{ \tfrac{1}{16}\left(1 + \frac{1-\gamma}{\gamma\mu}\right)^2 + \tfrac{1}{2}\left(\nu - \frac{1}{\gamma\mu}\right) \right\}^{1/2} \end{aligned} \tag{15}$$

In the parameter range of interest below ($\mu \approx 1$), only the upper sign yields a transition with $dv/dy < 0$. Notice, that at the sonic point $\frac{dv}{dy} = 1/a$ and $dT/dy = c/a = -1$. Equations (14) and (15) describe the behavior around the sonic point and numerical solutions can be obtained by starting with these initial conditions. We now wish to identify the relevant range of parameter values for C and μ. Evaluating Eq. (9) at the ablation front, one immediately finds,

$$C = T_1 + \frac{\gamma-1}{\gamma}\left(\frac{v_1^2}{2} + y_1\right) - \mu T_1^{\nu} \;\; . \tag{16}$$

Choosing the origin of the y-axis at the ablation front, $y_1 = 0$, the dominant term on the r.h.s. is $T_1 \ll 1$. Different values of C then correspond to solutions with different ablation front temperatures $T_1 \approx C$. The second parameter μ is the ratio of the sonic point temperature scale length $L_T = \chi_s/v_s$ over the scale height $L_s = T_s/mg$.

This suggests, that $\mu \lesssim 1$. For $\mu \ll 1$ the heat wave penetrates only a small fraction and for $\mu \approx 1$ a major fraction of the accelerated slab. We will now discuss in more detail these two limiting cases.

For $\mu \ll 1$ Eq. (9) allows a simple approximate solution,

$$\begin{aligned} T &= \left(-\frac{\nu}{\mu} y\right)^{1/\nu} \\ v &= 1 - \sqrt{1-T} \ . \end{aligned} \tag{17}$$

It is obtained by neglecting in the energy equation the small kinetic and potential energy terms as well as the constant C, and assuming consistently $|T'| \gg 1$ in the momentum equation. The solution (17) will be a good approximation up to the ablation front, where $T \approx T_1$. From Eq. (17) the Mach number near the ablation front is approximately $M = v/\sqrt{T} \approx \sqrt{T}/2 \ll 1$ and the ablation pressure, $p = \frac{T}{v} \approx 2$, about two times the sonic-point pressure. The parameter Γ of the instability analysis may be expressed as,

$$\Gamma = \mu v_1^{\nu-2} p_1^{\nu} \approx 2^{\nu} \mu v_1^{\nu-2} \ll 1 \ , \tag{18}$$

and can assume rather small values in this regime. Because of the steep temperature gradients the instability zone is likely to overlap the sonic point region, indicating that our results have to be modified for this case.

The opposite limiting case where $\mu \approx 1$ is more complicated and we therefore restrict attention to numerical solutions for $D_0 = 0$. Table 1 summarizes the ablation front parameters, obtained for some values of μ. For all cases of potential interest we actually find that $\mu \approx 1$ with deviations less than a few percent. The maximum ablation pressure now is only about $1.2\, p_s$, because of the pressure decrease due to the effective gravity. The distance d between the sonic point and the ablation front is about 0.4 and the instability parameter Γ varies between $0.1 - 0.3$. Steady-state profiles for the case where $\rho_1 = 50$, are displayed in Fig. 8. Near the ablation front (b) pressure variations are found small and the flow is well subsonic. One can therefore expect that compressibility effects here will only play a minor role for the instability evolution.

It may also be instructive to evaluate some steady-state parameters, which can easily be compared with experiments and simulations. We have seen that the source-free steady state requires $D_0 = 0$ and $\mu \approx 1$. The condition $\mu = 1$ determines therefore the characteristic accelerations g and scale heights L_s for a given sonic point temperature T_s. For an example, assuming classical electronic heat conduction, fully ionized carbon and a sonic point density of $10^{21}\mathrm{cm}^{-3}$ we refer to Fig. 9. Obviously, this case is too restrictive to account for the full variety of conditions in laser accelerated plasmas. However, allowing for an energy source at the sonic point this constraint can be dropped and steady-state solutions may be possible for $\mu \lesssim 1$. Then, at corresponding temperatures, the accelerations can be smaller and the scale lengths larger than those given in Fig. 9.

We finally wish to compare the present results with previous instability computations for compressible flows in spherical geometry.[7] Here the steady-state model is limited to source-free sonic-point transitions and the solutions are distinguished by two parameters $K_0 = \frac{\gamma}{\gamma-1}\mu/G$ and $G = r_1 r_s/L_s$, where r_1 is the radius of the ablation front in units of the sonic point radius r_s. Ablation front parameters, which we obtain for different values of K_0 and G are given in Table 2. The instability parameter,

$$\Gamma = \frac{\gamma-1}{\gamma} K_0 G r_1^6 \rho_1^{2-\nu} p_1^{\nu} \tag{19}$$

varies here in the small range between 0.1 and 0.2. In Ref. 7 the growth rates $\tilde{n} = n r_s/v_s$ are calculated as a function of the mode number ℓ. These are related to the present variables σ and κ by,

$$\tilde{n} = \frac{G}{\Gamma} r_1^2 \rho_1 \sigma \ , \ \ell = \frac{G}{\Gamma} r_1^5 \rho_1^2 \kappa \ , \tag{20}$$

where the approximate relation $k r_s = \ell/r_1$ has been used. As can be seen from Fig. 10 both results are in excellent agreement for large wave numbers. For small wave numbers the local analysis fails and shell-structure effects become important. Small discrepancies for density ratios $\rho_1 \lesssim 20$ are possibly related to the approximate relation $k r_s = \ell/r_1$ between the wave number k and the mode number ℓ.

Replacing the radius r_1 by the somewhat larger radius of the unstable layer will obviously yield better agreement in this case.

Finally it is noted, that the different profiles for $\rho_1 = 25$, $G = 2$ and $\rho_1 = 50$, $G = \sqrt{10}$ lead nearly to identical values of Γ. The corresponding growth rate curves are therefore represented by a single solution in the incompressible model. This confirms the fact that the instability evolution here is governed by the local profile structure.

Acknowledgments

The author wishes to thank P. Mulser and J. Meyer-ter-Vehn for continuous encouragement and support. Fruitful discussions with S.E. Bodner are gratefully acknowledged.

This research was supported by the Deutsche Forschungsgemeinschaft (Bonn, FRG).

References

1. S.E. Bodner, Phys. Rev. Lett. **33**, 761 (1974).
2. C.P. Verdon, R.L. McCrory, R.L. Morse, G.R. Baker, D.I. Meiron, and S.A. Orszag, Phys. Fluids **25**, 1653 (1982).
3. M.H. Emery, J.H. Gardner, and J.P. Boris, Phys. Rev. Lett. **48**, 677 (1982).
4. R.G. Evans, A.J. Bennett, and G.J. Pert, Phys. Rev. Lett. **49**, 1639 (1982).
5. H.J. Kull, and S.I. Anisimov, Phys. Fluids **29**, 2067 (1986).
6. R.L. McCrory, L. Montierth, R.L. Morse, and C.P. Verdon, Laser Interaction and Related Plasma Phenomena (Plenum, New York, 1981), Vol. **5**.
7. H. Takabe, L. Montierth, and R.L. Morse, Phys. Fluids **26**, 2299 (1983).

   H. Takabe, K. Mima, L. Montierth, and R.L. Morse, Phys. Fluids **28**, 3676 (1985).

Figure Captions

1. Steady-state density profiles as obtained from Eq. (2). The heat conductivity exponent increases by 1 for subsequent curves and is equal to 1 for the lowest curve.

2. Instability growth rates σ versus wave number κ.
   a) Growth rates for $\nu = 2.5$ and Γ varying from 0.01 to 100.
   b) Growth rates for $\Gamma = 0.2$ and $\nu = 2.5$, 5, and 8.

3. Instability boundary $\kappa_c = \kappa_c(\Gamma)$. It increases faster than Γ for $\Gamma \ll 1$ and slower than $\sqrt{\Gamma}$ for $\Gamma \gg 1$.

4. Spatial mode structures for different wave numbers κ with $\Gamma = 0.17$ and $\nu = 2.5$. The different curves represent the variables Y_i defined by Eq. (4) and are labeled by the index i. The variable Y_4 has been divided by a normalization constant c. a) $\sigma = 0.012$, $c = 100$, b) $\sigma = 0.015$, $c = 50$, and c) $\sigma = 6.10^{-5}$, $c = 20$.

5. Local mode structure for boundary layers with increasing width d. The results are displayed as explained in Fig. 4 with $c = 10$. The variables Y_i are continuous across a sharp front, but vary in the interior if $d \gtrsim 1$.

6. Comparison of a) the variables Y_i, with b) $\overline{\delta\rho}$ $-\cdot-\cdot$, $\delta\bar{p}$ $---$, $ic\delta\bar{v}_x$ — and $\delta\bar{v}_y$ $\cdots$. The parameters are $\Gamma = 0.1$, $\bar{\rho}_2 = 0.1$, $\kappa = 0.02$, $\kappa d = 0.01$ and $\sigma = 0.02$. The normalization constant of Y_4 is $c = 10$.

7. Sharp-boundary mode structures for the same parameter values as in Fig. 4.
   a) $\sigma = 0.012$, $c = 10$,
   b) $\sigma = 0.015$, $c = 10$,
   c) $\sigma = 8.10^{-5}$, $c = 1$.

8. Steady ablation front with $\rho_1 = 50$ and $D_0 = 0$.
   a) The ablation front ($d\rho/dy = 0$) is well separated from the sonic point ($M = 1$).
   b) Near the ablation front pressure variations are small compared with the density variations and the flow is well subsonic.

9. Typical steady-state parameters g and L_S as a function of T_S for extended fronts ($\mu = 1$).

10. Comparison of present incompressible (——) and previous compressible (– – –) results. For sufficiently large mode numbers, where the local analysis becomes valid, excellent agreement has been obtained. The dotted line gives the standard RT growth rate $\propto \sqrt{\ell}$ without ablation.
    a) $G = \sqrt{10}$, $\rho_1 = 50$
    b) $G = 2$, $\rho_1 = 12.5, 25, 50, 100$.

Table 1: Plane ablation fronts

μ	ρ_1	T_1	p_1	$\lvert y_S \rvert$	Γ
0.922	10	0.1	1.01	0.447	0.296
0.975	20	0.055	1.11	0.424	0.284
0.995	30	0.039	1.16	0.416	0.263
1.012	50	0.024	1.20	0.410	0.225
1.025	100	0.012	1.24	0.406	0.175
1.032	200	0.006	1.25	0.405	0.129
1.036	500	0.003	1.26	0.403	0.082

Table 2: Spherical ablation fronts

G	K_0	ρ_1	T_1	p_1	r_1	Γ
$\sqrt{10}$	0.5195	50	0.03	1.54	0.924	0.171
2	0.6225	12.5	0.12	1.47	0.892	0.184
2	0.6605	25	0.06	1.56	0.899	0.170
2	0.6810	50	0.03	1.63	0.903	0.140
2	0.6913	98	0.017	1.70	0.904	0.115

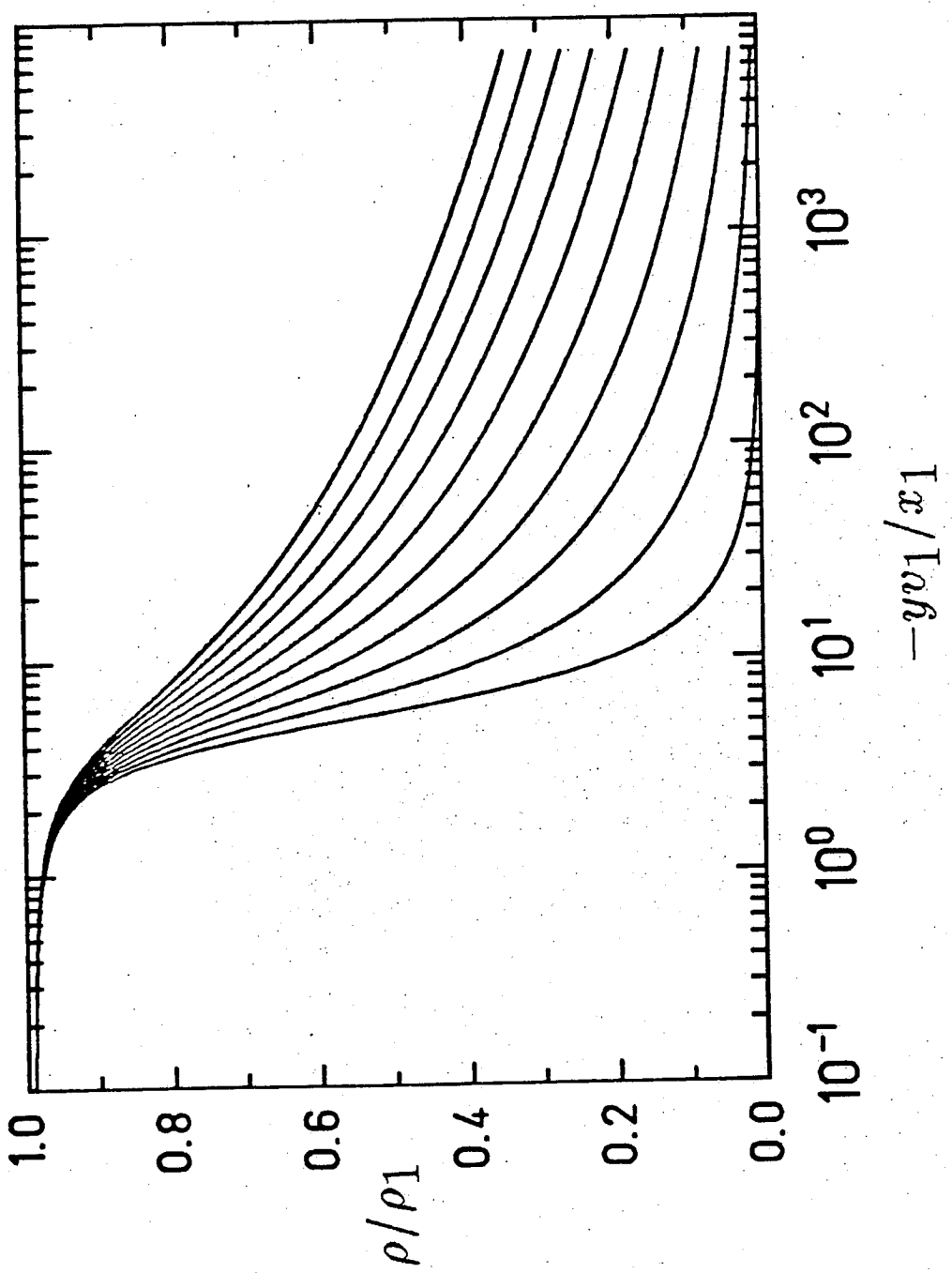

Fig. 1

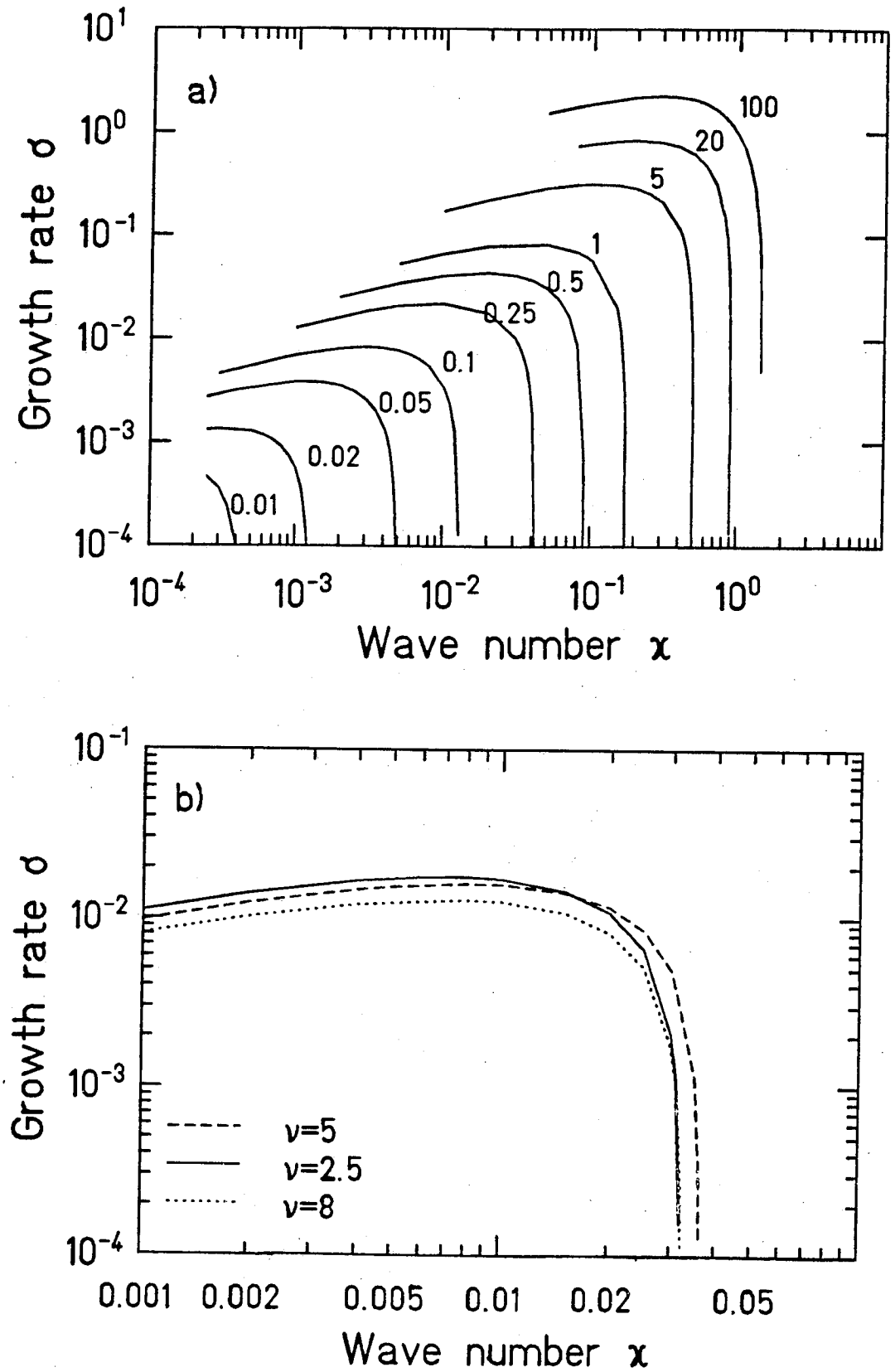
a)
Growth rate σ
Wave number χ
100
20
5
1
0.5
0.25
0.1
0.05
0.02
0.01
b)
ν=5
ν=2.5
ν=8

Fig. 2

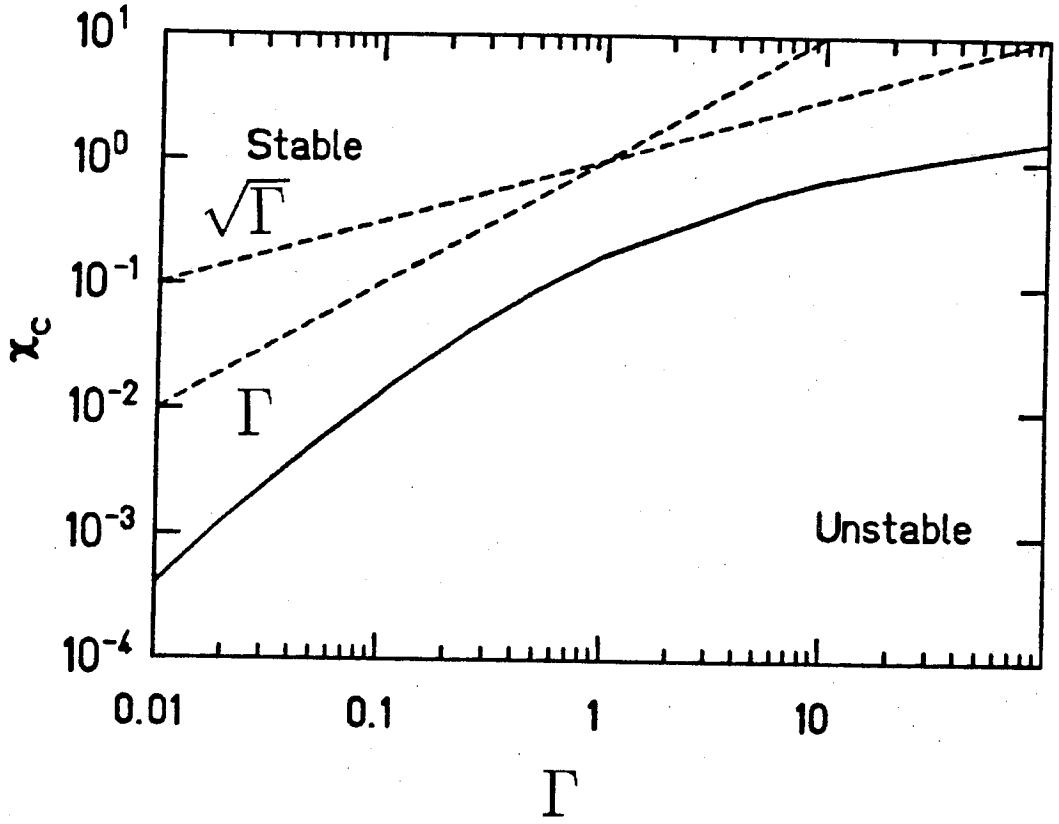
10^1
10^0
10^{-1}
10^{-2}
10^{-3}
10^{-4}
χ_c
Stable
$\sqrt{\Gamma}$
Γ
Unstable
0.01
0.1
1
10
Γ

Fig. 3

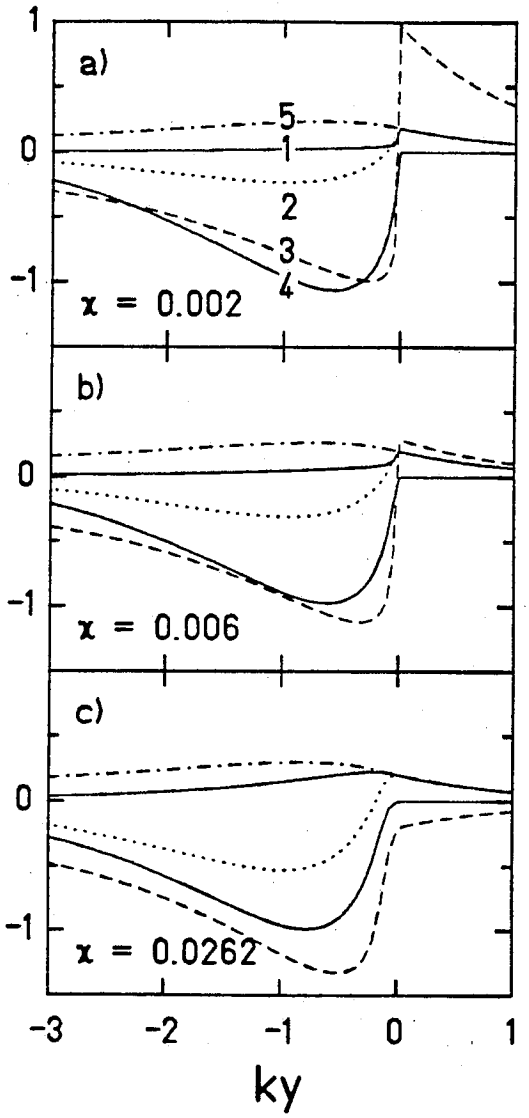

Fig. 4

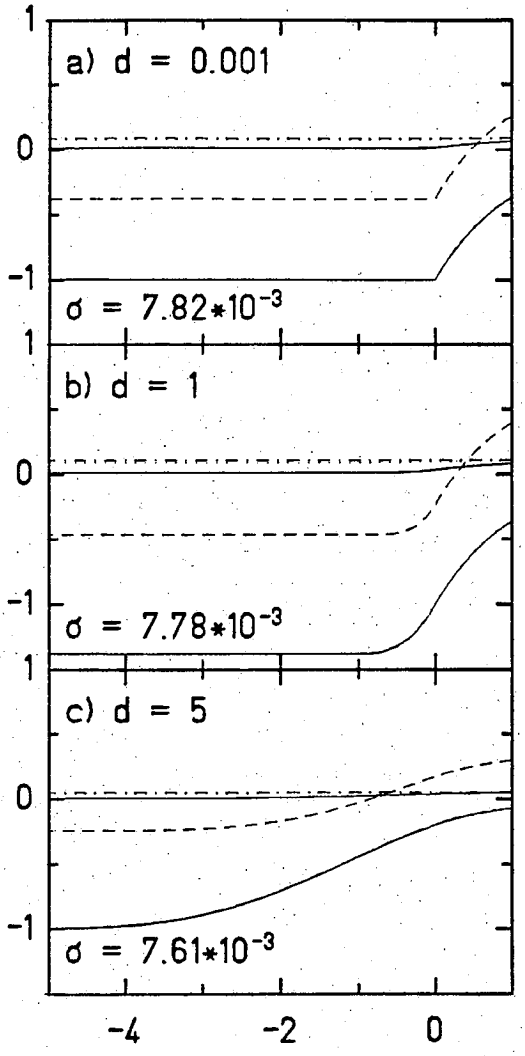

Fig. 5

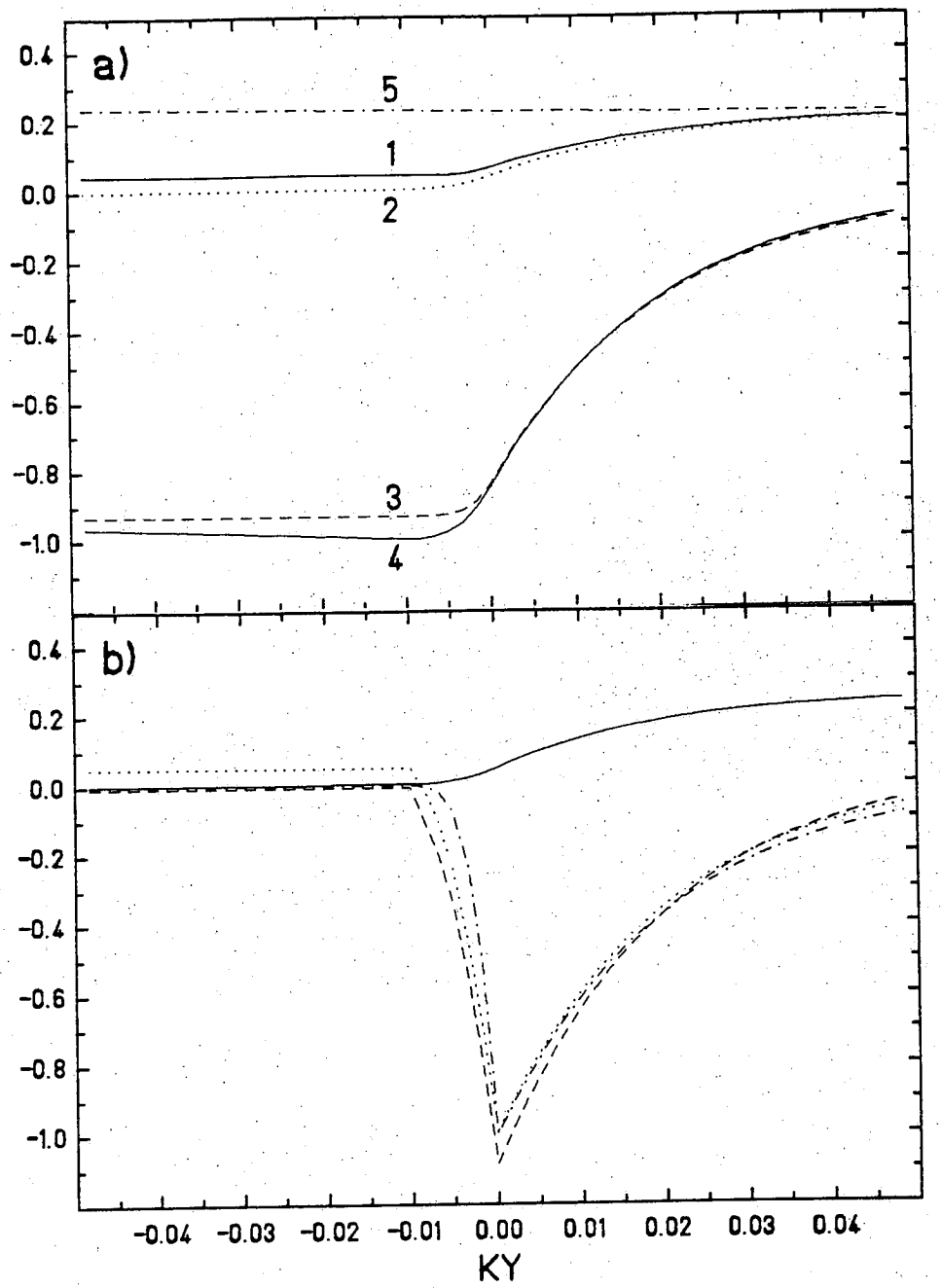
a)
b)
5
1
2
3
4
0.4
0.2
0.0
-0.2
-0.4
-0.6
-0.8
-1.0
-0.04
-0.03
-0.02
-0.01
0.00
0.01
0.02
0.03
0.04
KY

Fig. 6

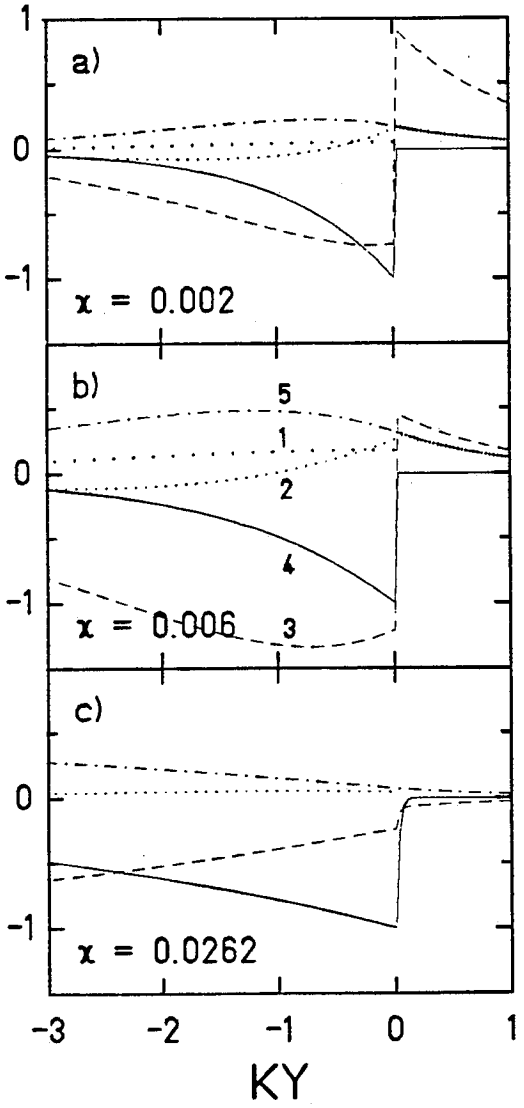

Fig. 7

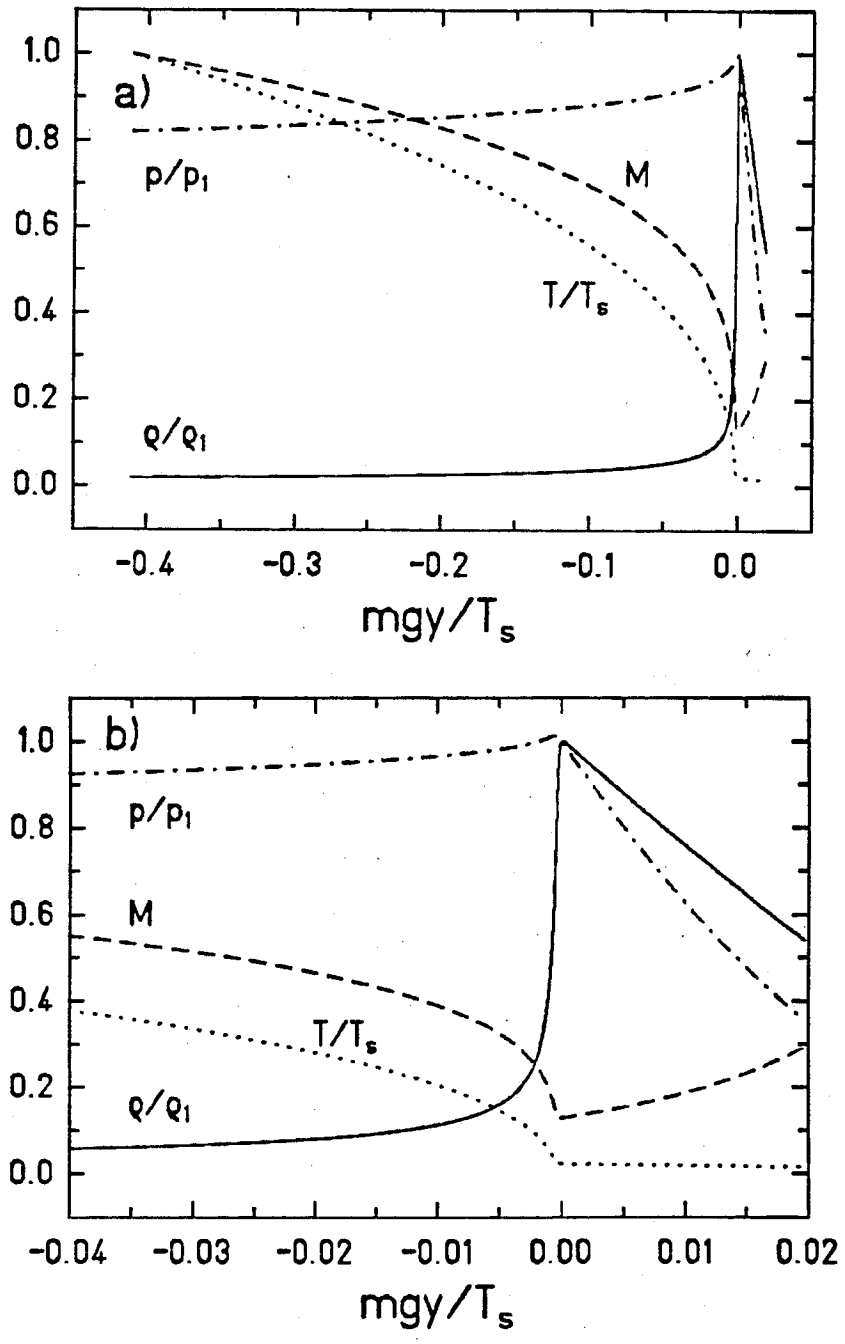
a)
p/p1
M
T/Ts
ρ/ρ1
1.0
0.8
0.6
0.4
0.2
0.0
-0.4
-0.3
-0.2
-0.1
0.0
mgy/Ts
b)
p/p1
M
T/Ts
ρ/ρ1
1.0
0.8
0.6
0.4
0.2
0.0
-0.04
-0.03
-0.02
-0.01
0.00
0.01
0.02
mgy/Ts

Fig. 8

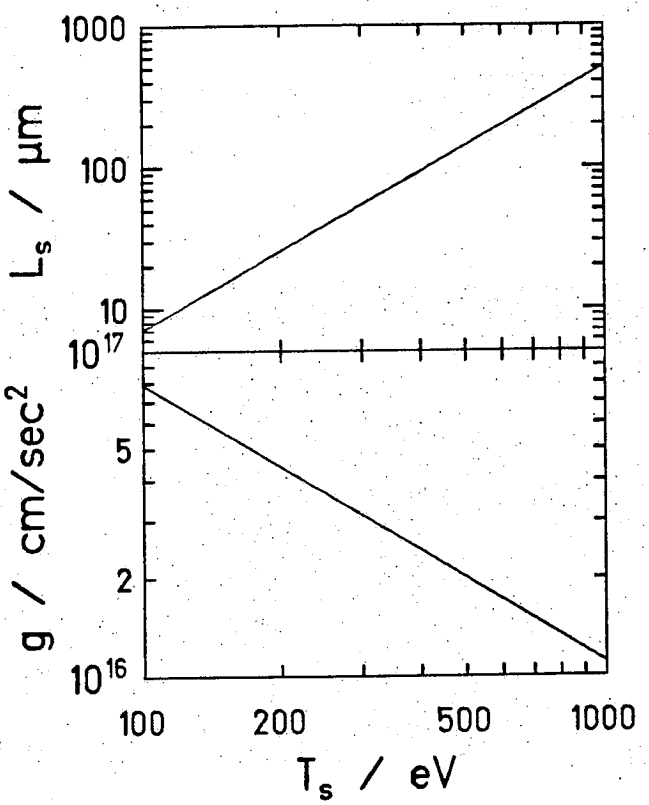

Fig. 9

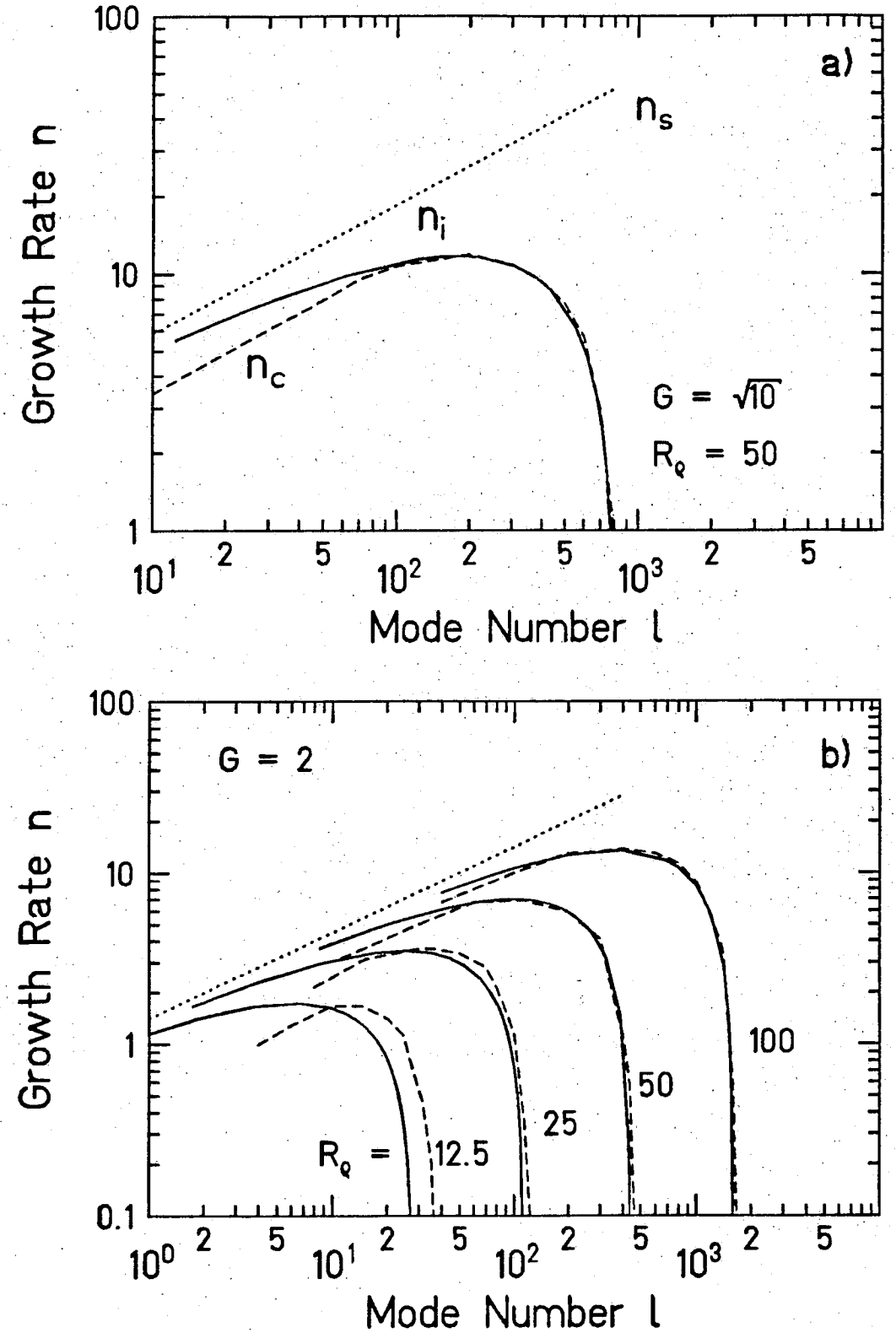
a)
100
10
1
Growth Rate n
n_s
n_i
n_c
G = √10
R_Q = 50
10^1
2
5
10^2
2
5
10^3
2
5
Mode Number l
b)
G = 2
100
10
1
0.1
Growth Rate n
R_Q =
12.5
25
50
100
10^0
2
5
10^1
2
5
10^2
2
5
10^3
2
5
Mode Number l

Fig. 10